



# Multi-site near-infrared tomographic imaging of the brain

D. P. Klemer<sup>1</sup>, R. L. Barbour<sup>1</sup>, C. H. Schmitz<sup>1</sup>, H. L. Graber<sup>1</sup>, Y. Pei<sup>2</sup>, R. E. Hardin<sup>1</sup>, M. S. Katz<sup>1</sup>, N. A. Franco<sup>1</sup>, A. G. Smeraldi<sup>3</sup>, A. Di Martino<sup>4</sup>, F. X. Castellanos<sup>4</sup>  
<sup>1</sup>SUNY Downstate Medical Center, <sup>2</sup>NIRx Medical Technologies, LLC., <sup>3</sup>Staten Island University Hospital, and <sup>4</sup>NYU Child Study Center



## INTRODUCTION

Dynamic near-infrared optical tomography is presently being applied to investigations of vascular compliance, benign and malignant breast lesions, and vascular correlates of brain functioning. The relationships between activation of neural tissue and the associated reactions of its vascular supply have made task-related hemodynamics a key focus of neuroimaging studies.<sup>1,2</sup> Two methods that are particularly suitable for examining vascular dynamics are functional magnetic resonance imaging (fMRI)<sup>3</sup> and near-infrared spectroscopy (NIRS).<sup>4</sup> In recent years the NIRS method has been refined to incorporate array sampling techniques for the purpose of generating 2D topographic (i.e., surface maps),<sup>5</sup> and more recently, 3D tomographic images.<sup>7</sup> Compared to fMRI, the NIRS technique offers improved temporal resolution and unambiguous discrimination of the components of the hemoglobin (Hb) signal (i.e., oxy-, deoxy-, and total hemoglobin). On the other hand, the NIRS technique is less capable than fMRI of probing brain structures beyond 3-4 cm in depth, and its spatial resolution is typically lower.

Tomographic imaging with near-infrared (NIR) radiation was first proposed in the late 1980's as a static imaging method.<sup>8</sup> Beginning in the late 1990's, our group first demonstrated the practicality of extending the NIR imaging technique, also known as diffuse optical tomography (DOT), to capture time series data to explore the vascular dynamics of large tissue structures.<sup>9</sup> In the ensuing years we have undertaken an extensive technology development effort to produce a general-purpose imager suitable for examining a range of tissues including the brain. Instrumentation design,<sup>10</sup> reconstruction algorithms for fast, stable image recovery,<sup>11</sup> time-series image analysis,<sup>12</sup> and approaches for system calibration and data integrity<sup>13</sup> have been described in various reports.

In this report we present preliminary findings obtained while using our time-series imager to explore the vascular response of the brain to several types of neural activation. These pilot studies include an examination of the focal vascular response to finger-tapping<sup>3</sup> as measured over the motor cortex in one study, over the motor and frontal cortex in a second study, and over a range of locations in a third study that also included several verbal tasks and a respiratory task in the traditional boxcar design. As will be shown, even these preliminary results demonstrate the wealth of data available with increasingly sophisticated NIRS approaches.

## THE INSTRUMENTATION

A multi-channel continuous wave near-infrared optical tomographic imager (DYNOT System, NIRx Medical Technologies, LLC., Glen Head, NY 11545), operating at 760 nm and 830 nm, was used for all measurements. In Figure 1 we show a functional layout of the imager with expanded views of the instrument set-up and real-time data display screens. Depicted is a four-level functionality scheme comprising system hardware, system control, data analysis and image display. The basic system provides for frequency encoding having a capability of up to four laser diode sources, a fast optical switch with incoupling optics, use of various measuring heads, a multichannel parallel detector module equipped with adjustable gain control, and a system controller.

Dynamic measurements were performed using a measurement head which directs near-infrared light onto the subject's scalp via multiple arrays of optical fibers mounted in a secure frame. Each optode delivers approximately 20 mW of optical power for a period of 10 ms per cycle, producing a flux of  $\sim 10 \text{ mJ s}^{-1} \text{ cm}^{-2}$ . Dual-wavelength optical energy at wavelengths 760nm and 830nm was used for imaging in a time-multiplexed fashion, such that a complete scan of the arrays is accomplished in approximately 400 milliseconds. Figure 2 shows a close-up view of the measuring head, which allows for flexible array geometries, that was used for these neuroimaging studies.

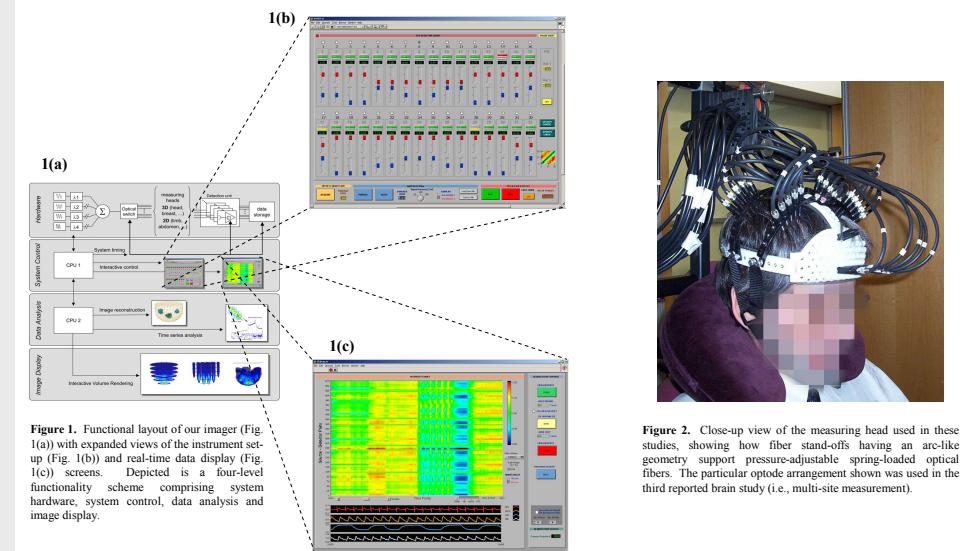


Figure 1. Functional layout of our imager (Fig. 1(a)) with expanded views of the instrument set-up (Fig. 1(b)) and real-time data display (Fig. 1(c)) screens. Depicted is a four-level functionality scheme comprising system hardware, system control, data analysis and image display.



Figure 2. Close-up view of the measuring head used in these studies, showing how fiber stand-offs having an arc-like geometry support pressure-adjustable spring-loaded optical fibers. The particular optode arrangement shown was used in the third reported brain study (i.e., multi-site measurement).

Use of time-multiplexing methods necessarily limits the data acquisition rate by a factor that depends on the number of illumination sites in the sensor array. In practice, we can achieve image framing rates on the order of 2-3 Hz for a 32x32 sensor array, which is more than sufficient for capturing the relevant dynamics of most vascular-related events.<sup>13</sup> Higher acquisition rates are achievable if fewer source locations are used, up to a limit, using present hardware, of 90 Hz. Additionally, we employ frequency-coding methods to provide for simultaneous illumination at all wavelengths at one site to avoid temporal biases when collecting data with more than one wavelength.

## NEUROIMAGING EXPERIMENTAL PROTOCOLS

**Experiment 1 – Motor Cortex**  
For the initial brain imaging study, we targeted activation of the motor cortex in response to contralateral finger tapping, using a boxcar design. Data were collected in parallel from 24 channels, at a source switching rate of 2.5 Hz. The optodes were configured in a rectangular pattern (6x4 cm) that provided up to 576 independent source-detector channels, positioned over the left scalp (See Figure 3(a)). After 320 s of a resting baseline period, the subject alternated 3 block periods (~40 s each) of right hand four-finger flexion/extension (at 1 Hz) with 3 quiet resting blocks (~40 s each).

**Experiment 2 – Motor and Anterior Frontal Cortices**  
Measurements were recorded from a second subject while using a similar boxcar finger-tapping sequence. Thirty optodes were distributed between two sub-arrays of 15 optodes each (Fig. 3(b)). Resting baseline data were acquired over an interval of ~600 seconds, after which the subject performed a sequence of motor and cognitive tasks. The motor tasks consisted of a sequence of 5 epochs of rhythmic finger tapping (~40 s each) alternating with quiet rest periods of the same duration.

**Experiment 3 – Multi-site Recording**  
The third subject participated in a series of pilot tasks with the optodes placed on the head in a widely distributed manner. Six groups of 5 optodes each were arranged in linear arrays (Fig. 3(c)). Each of the 6 sites was limited to 25 source-detector channels (5 sources by 5 detectors), which is insufficient for adequate image recovery; thus, analyses in this study were limited to spectroscopy. Adjacent fibers within each line were separated by ~1 cm. Three of the linear arrays were over the left frontolateral, centro-temporal, and temporal-parietal areas of the scalp. Two linear arrays overlay the right frontolateral and temporal areas of the scalp. The sixth line was placed horizontally over the forehead, with one fiber on the midline, three on the left, and one on the right side.

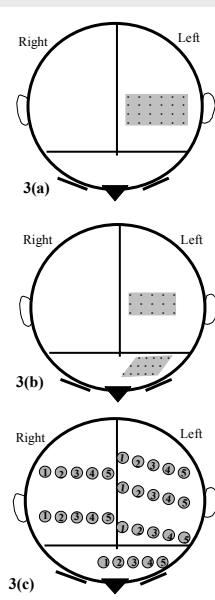


Figure 3. Schematic representations of the optode pattern used in the three experiments. 3(a): rectangular (6x4 cm) 24 optode pattern, positioned on the left side of the head, overlying the area corresponding to the hand motor cortex according to the 10-20 EEG system. 3(b): 15-optode patterns (each about 5x3 cm) used in simultaneous dual-site measurement. 3(c): six five-optode linear array pattern used for the multi-site experiment.

## NEUROIMAGING EXPERIMENTAL PROTOCOLS (cont.)

**Experiment 3 – Multi-site Recording (cont.)**  
After a resting baseline period of ~540 s, the subject performed a sequence of motor, cognitive, and respiratory tasks. The motor tasks consisted of two sequences of four epochs (each ~30 s) of rhythmic finger tapping alternating with five quiet resting periods (each ~30 s), first with the right hand and then with the left. The first cognitive task comprised four epochs (each ~30 s) of out-loud reverse-order word reading alternating with five quiet resting periods (each ~30 s). The second comprised four epochs of out-loud forward-direction recitation of the English alphabet (each ~30 s), alternating with five quiet rest periods (each ~30 s); the third was similar to the second, except that the alphabet was recited in reverse order. The respiratory task consisted of four Valsalva maneuvers (each ~30 s) alternating with five recovery epochs (each ~60 s).

## DATA PROCESSING

The following are brief synopses of the analytical steps used in data processing.

**1. Data Pre-Processing.** Raw data were first low-pass filtered for experiments 1 and 3, with threshold frequencies of 0.15 Hz and 0.3 Hz, respectively, to minimize cardiac signals and improve signal/noise. Coefficients of variation (CV) were computed for the baseline-period data points in each source-detector channel's data time series, for each of the two wavelengths. Only channels with CV values below 15% (experiments 1 and 3) or 20% (experiment 2) for both wavelengths were used in subsequent analyses. Raw data for all remaining channels were normalized based on the time-varying laser intensity recorded during the experiment, then were further normalized based on the mean value recorded during the baseline period. During this step, an adaptive median filtering algorithm was applied, as needed, to eliminate negative instantaneous values resulting from measurement noise.

**2. Image Reconstruction.** Where indicated, image recovery was achieved using the Normalized Difference Method.<sup>14</sup> As previously shown, this algorithm is markedly insensitive to expected uncertainties in boundary conditions, which are inherent to experimental methods. A truncated singular value decomposition procedure to solve the linear perturbation equation, as described elsewhere,<sup>15</sup> The absorption coefficient images were subsequently post-processed to produce image time series for oxygenated, deoxygenated, and total hemoglobin (Hb) concentration changes.

**3. Computation of Hemoglobin States.** In all cases, the mean value of Hb concentration during the initial resting baseline period was set to an arbitrary constant. A modified Beer-Lambert law,<sup>16</sup> applied to the logarithms of the two-wavelength normalized detector readings, was used to compute estimates of the time-dependent fluctuations in concentrations of oxy-Hb and deoxy-Hb, and of total Hb concentration, in the tissue probed by each source-detector channel. In time-series of reconstructed images, the corresponding changes in Hb concentration were computed from the reconstructed two-wavelength absorption coefficients at each node, by solving a simple algebraic system of two equations in two unknowns.<sup>17</sup>

**4. Multivariate Signal Analysis.** For each study, subsets of the Hb-concentration data for the time intervals corresponding to the various boxcar protocols (i.e., alternating epochs of task performance and rest) were isolated from the complete time series. These were processed with a general linear model (GLM) algorithm<sup>12</sup> that found the best fit of each time series in these data subsets to a linear combination of four model functions (i.e., a four-column design matrix), as schematically illustrated in Figure 4. The four model functions used were a constant (offset) term, linear and quadratic baseline drift functions, and a two-state boxcar function that follows the ideal sequence of transitions between task and rest epochs. All four models were normalized to unit Euclidean length, and all but the first were mean-subtracted. Subsequently, the percent-of-variance accounted for (PVA) in each channel's or finite element method mesh node's time series was computed, as the coefficient of determination between the boxcar model and the de-trended channel or pixel data. It should be noted that none of the subsequently presented results of these analytical steps have been thresholded, and that we did not compute average responses across epochs prior to performing the GLM computations.

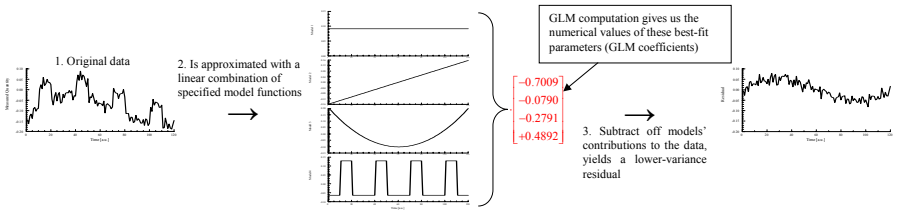


Figure 4. Schematic illustration of the action of a GLM computation.

## RESULTS

**Motor Cortex.** Local neuronal activation is expected to produce an event-related increase in blood flow causing an increase in blood volume with improved oxygenation.<sup>3,4</sup> In Figure 5 we show a 3D map (7.5x5x4 cm<sup>3</sup>) of the value of the GLM coefficient of the boxcar model function, for oxy-Hb and deoxy-Hb. Shown in Fig. 5(a) and 5(b) are the oxy-Hb and deoxy-Hb responses, respectively, during the task or activation period. Inspection reveals a focal activation occurring in the area of the motor cortex that is approximately six times greater than the response for deoxy-Hb, a finding consistent with a focal increase in blood flow. The 3D resolving capability of our technique is demonstrated by Fig. 5(c) which shows a side view of the result seen in Fig. 5(a). Clearly evident is a localized response which appears to occur at a depth of ~0.5-1 cm below the surface. As a control, the maps shown in Fig. 5(d) and 5(e) are the corresponding GLM results computed by applying the boxcar model function to the baseline period, revealing a more diffuse response with reduced amplitude.

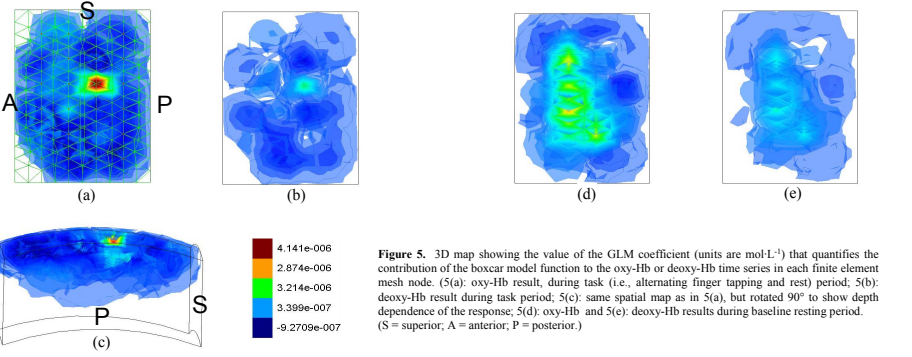


Figure 5. 3D map showing the value of the GLM coefficient (units are mol.L<sup>-1</sup>) that quantifies the contribution of the boxcar model function to the oxy-Hb or deoxy-Hb time series in each finite element mesh node. (a): oxy-Hb result, during task; (b): deoxy-Hb result, during task; (c): same spatial map as in (a), but rotated 90° to show depth dependence of the response; (d): oxy-Hb results during baseline resting period; (e): deoxy-Hb results during baseline resting period. (S = superior, A = anterior, P = posterior)

**Motor and Anterior Frontal Cortices.** In order to explore the ability of the instrument to record from two distinct regions that may be functionally linked, we used the same basic task parameters, with the array divided into two groups as shown in Fig. 3(b). The results shown in Figure 6 illustrate a typical temporal response profile extracted from the oxy-Hb signal detected with the 3x5 frontal array. The data in this figure represent the first principal component<sup>12</sup> of the oxy-Hb signal during the 400-s finger-tapping task; oscillations in oxy-Hb levels are clearly coincident with the boxcar model function shown. In Figure 7(a) we illustrate mean temporal oxy-Hb responses for both the motor and frontal arrays, together with their cross-correlation function, for the 400 seconds corresponding to the duration of the finger-tapping experiment. The results reveal prominent boxcar responses at both sites, and these responses are strongly time-correlated, indicating tight temporal coordination. As a control, Figure 7(b) shows the result of similar analysis applied to 400 seconds during the initial baseline period; the baseline temporal fluctuations in the mean oxy-Hb responses for the two arrays are mainly uncorrelated.

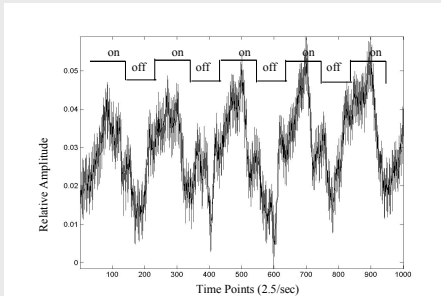


Figure 6. Temporal response of the oxy-Hb signal (first principal component) during finger-tapping sequence.

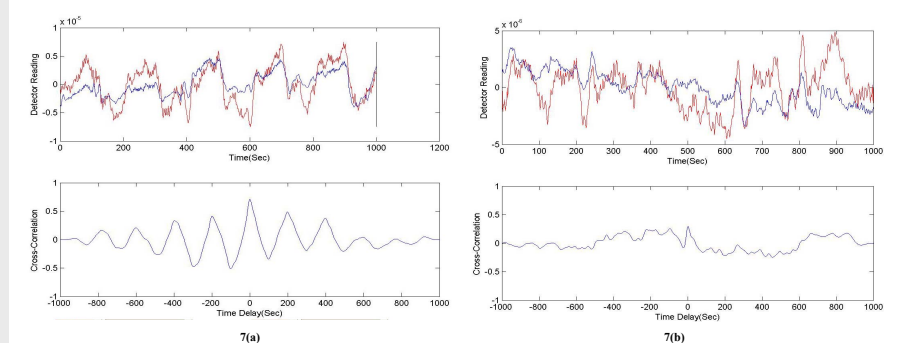


Figure 7. 7(a): Spatially-averaged oxy-Hb temporal responses (top) associated with frontal (red) and motor (blue) arrays, for the duration of the finger-tapping sequence. Bottom: cross-correlation between frontal and motor signals. 7(b): identical measurement as in Fig. 7(a), recorded during a 400 second subset of the initial baseline period.

We next illustrate a GLM calculation that used the mean oxy-Hb time series as a model function. Figure 8(a) shows the spatial distribution of the coefficients corresponding to the model fit, across the three-dimensional volume of brain imaged by the frontal array. It is clear that a focal region of activity exists, slightly below the surface. Similar GLM analyses for the motor array illustrate a clear focal region of activity as well, shown in Figure 8(b), where the mean oxy-Hb time series of the motor array was used as a model function for the GLM analysis.

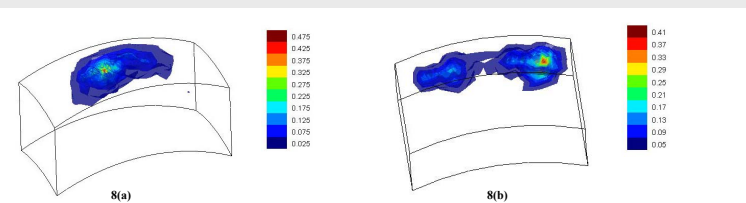


Figure 8. 8(a): Three-dimensional image of the spatial portion of the first principal component (PC) of the oxy-Hb time series associated with the frontal cortex array. 8(b): similar image for the first PC oxy-Hb time series associated with the motor cortex array.

**Multisite Recording.** As noted above, this third experiment was conducted with six widely separated linear arrays of five optodes each; additionally, the activation paradigms included focal motor tasks, three verbal tasks, and Valsalva maneuvers. Figure 9 illustrates a representative oxy-Hb and deoxy-Hb time series associated with a single source-detector channel; the various activation paradigms are illustrated.

The GLM algorithm was applied to all source-detector channels, and those channels yielding significant Bonferroni-corrected positive or negative GLM coefficients were noted. (The model function employed was a boxcar function applied to oxy-Hb, deoxy-Hb, and derived total Hb.) In this analysis, each linear array yielded 25 source-detector pairs (channels). During finger tapping tasks, a minority of the channels yielded significant correlations with the boxcar model (27% of the 300 possible channel-Hb states for right hand, 14% for left hand). By contrast, during backward reading out loud, 63% of the possible values resulted in significant correlations with the boxcar model. This value increased to 82% and 81% for forward and backward recitations from memory of the English alphabet, respectively. Similarly, Valsalva maneuvers produced significant correlations with the boxcar function in 266 out of 300 (89%) possible values. Thus the language tasks and the respiratory manipulation provoked much more widespread alterations in time-locked Hb concentrations than the focal finger tapping tasks. Moreover, it is seen that the patterns of positive and negative correlations are more similar among the three language tasks than between any of the latter and the Valsalva maneuver task. This finding supports the inference that the behavior observed during the language tasks is not simply a manifestation of the blood pressure changes that occur when the subject speaks.

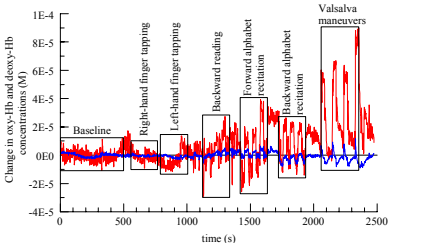


Figure 9. Representative oxy-Hb (red) and deoxy-Hb (blue) detector time series showing the various activation paradigms for the Multisite Recording experiment.

Figure 10(a) illustrates the average of the oxy-Hb data for all 25 source-detector channels associated with the left centro-temporal array (green) and left frontolateral array (brown). Figure 10(b) illustrates the analogous data for deoxy-Hb. The two arrays clearly manifest qualitatively different behavior, on both slow and fast time scales; the magnitudes of dynamic changes during the various activation paradigms is evident when comparing the traces in 10(a) and 10(b).

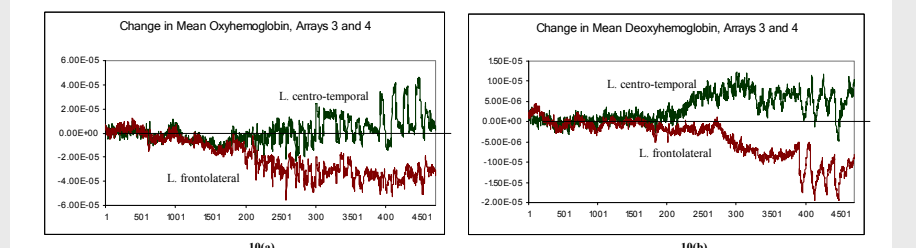


Figure 10. Spatially-averaged oxy-Hb (10(a)) and deoxy-Hb (10(b)) temporal responses associated with two individual neuroimaging arrays.

Although the optode arrays were not located in a fully symmetrical manner, we examined approximate hemispheric asymmetries by combining the left frontolateral and centro-temporal arrays and comparing them to their right frontolateral and centro-temporal counterparts. Table 1 shows that those source-detector pairs covered over the left hemisphere resulted in a significantly higher number of positive GLM coefficients—indicating that the response seen in the respective hemoglobin signal was positively correlated with the boxcar model—as compared to those over the right hemisphere for both the individual oxygenation states of Hb and for total Hb (i.e., blood volume) during the verbal/language tasks. By contrast, the two hemispheres did not differ significantly in the number of significant negative GLM coefficients. Likewise the Valsalva maneuvers, which resulted in the highest number of significant GLM coefficients, did not differ significantly in the proportion of right versus left channels yielding significant coefficients. Nineteen channels yielded significantly positive coefficients for oxy-Hb during right handed finger tapping, versus two channels during left-handed finger tapping; the corresponding numbers for negative coefficients were 5 and 6, respectively ( $p = 0.03$ , Fisher's exact). Similarly, a significantly higher number of channels showed significant negative coefficients for deoxy-Hb with right handed tapping (14, versus 3 for left handed tapping), whereas the numbers of channels with significantly positive coefficients barely differed (18 right, 17 left; overall  $p = 0.02$ , Fisher's exact).

Table 1. Table entries are the total number of source-detector channels that yielded significant GLM coefficients during verbal tasks in left versus right frontolateral and centro-temporal linear arrays.

	Oxy-Hb	Oxy-Hb	Deoxy-Hb	Deoxy-Hb	Total-Hb	Total-Hb
	+b	-b	+b	-b	+b	-b
<b>Left hemisphere</b>						
Total number of channels	21	116	53	77	36	106
<b>Right hemisphere</b>						
Total number of channels	3	119	26	80	7	122
<b>Fisher's exact p</b>	<b>0.0004</b>		<b>0.009</b>		<b>0.00007</b>	

## CONCLUSIONS

The purpose of these pilot studies was to explore the utility of a prototype multi-channel continuous wave near-infrared optical tomographic imager for detecting hemodynamic changes occurring in the brain during various types of mental and physiological tasks. As others have previously shown and our first experiment showed that the measurement system appears to detect changes in cerebral blood oxygenation related to focal cortical activation provoked by motor activity, as indexed by increased [oxy-Hb] and decreased [deoxy-Hb] during finger tapping. Further, this initial study suggests that the tomographic approach we have adopted will support a desirable level of 3D resolution. In Experiment 2 we were able to detect synchronized hemodynamic fluctuations during the boxcar period that were absent during the resting baseline. Examination of such correlated activity may yield insights into functional connectivity of distributed brain circuits.<sup>20</sup> In Experiment 3 we performed a highly rudimentary study approaching a whole cortex scan, along with a wide range of tasks from highly focal finger tapping, to verbal reading, recitation, and Valsalva maneuvers. We found that the focal motor tasks did in fact result in many fewer "active" source-detector channels (defined as those channels with significant positive or negative correlations/coefficient with the boxcar function) than did the tasks that required verbal output responses. This response mode, which is not possible during fMRI studies because of the deleterious effects of motion on signal noise (particularly in the longitudinal axis) and of changing susceptibility artifacts as the oral cavity changes, is of great interest for NIRS studies. We tentatively conclude that we observed a relatively global shunting of blood towards the left anterior hemisphere during the verbal tasks. Whether this asymmetry was related to the tasks entailing language, or to verbal output, or to the effortful nature of the tasks, is unclear from the present design. Thus this pattern of findings will serve as the basis for more targeted hypothesis testing with more rigorously designed cognitive and motoric/physiological control conditions. Overall, these pilot data suggest that the prototype tomographic imager that we have developed is able to measure spatially heterogeneous variations in brain hemodynamic activity. Future iterations will benefit from an expanded number of optodes as well as substantially larger numbers of subjects. We believe that continued development will result in instruments that will not seek merely to compete with fMRI, but will expand the nature and range of questions about brain activity that can be addressed through this nascent technology.

## REFERENCES AND ACKNOWLEDGEMENTS

1. D. A. Beusans, S. R. Hinz, A. Villringer, D. Boas, A. Klenk-Schmidt, J. Frahm, C. Harh, H. Obrig, J. C. van Houten, E. L. Kernt, W. F. Cheng, and D. K. Stevenson, "Noninvasive functional imaging of human brain using light," *J. Cereb. Blood Flow Metab.* **20**, 469-477 (2000).
2. M. A. Franceschini and D. A. Boas, "Noninvasive measurement of neuronal activity with near-infrared optical tomography," *Neuroimage* **21**, 372-380 (2004).
3. C. Strangman, J. P. Culver, J. H. Thompson, and D. A. Boas, "A quantitative comparison of simultaneous BOLD fMRI and NIRS recordings during functional brain activation," *Neuroimage* **17**, 719-731 (2002).
4. R. B. Buxton, *Introduction to Functional Magnetic Resonance Imaging: Principles and Techniques*, Cambridge University Press, Cambridge, (2002).
5. Q. Luo, S. Zeng, B. Chance, and S. Nioka, "Monitoring of brain activity with near-infrared spectroscopy," Chap. 8 in *Handbook of Optical Biomedical Diagnostics*, V. V. Tuchin, Ed., SPIE Press, Bellingham, WA (2002).
6. G. Gratton and M. Fabiani, "The event-related optical signal: a new tool for studying brain function," *Int. J. Psychophysiol.* **42**, 109-121 (2001).
7. A. Y. Bluestone, G. Abdolmalek, C. H. Schmitz, R. L. Barbour, and A. H. Heisler, "Three-dimensional optical tomography of hemodynamics in the human head," *Optics Express* **9**, 272-286 (2001).
8. R. L. Barbour, H. L. Graber, R. Anzures, and J. Labovsky, "Model for 3-D optical imaging of tissue," *International Conference and Remote Sensing Symposium (IGARSS)*, **2**, 1395-1399 (1990).
9. R. L. Barbour, H. L. Graber, C. H. Schmitz, Y. Pei, S. L. S. Zhong, S. L. S. Barbour, S. Blattman, and T. Panetta, "Spatio-temporal imaging of vascular reactivity by optical tomography," *Proceedings of Inter-institutional Workshop on In Vivo Optical Imaging at the NIAA*, H. Gandjbakhche, Ed., pp. 161-166, Optical Society of America, Washington, DC (1999).
10. C. H. Schmitz, H. L. Graber, H. B. Luo, A. J. Anzures, Y. Pei, A. Bluestone, S. Zhong, R. Andronico, I. Solter, S. Ramirez, S. L. S. Barbour, and R. L. Barbour, "Instrumentation and calibration protocol for imaging dynamic features in dense-scattering media by optical tomography," *Applied Optics* **39**, 6666-6680 (2000).
11. Y. Pei, H. L. Graber, and R. L. Barbour, "Normalized-constraint algorithm for minimizing inter-parameter crosstalk in DC optical tomography," *Optics Express* **9**, 97-109 (2001).
12. H. L. Graber, Y. Pei, R. L. Barbour, D. K. Johnston, Y. Zheng, and J. E. Mayhew, "Signal source separation and localization in the analysis of dynamic near-infrared optical tomographic time series," *Proceedings of SPIE Optical Tomography and Spectroscopy of Tissue V*, B. Chance, R. R. Alfano, B. J. Tromberg, M. Tamura, and E. M. Sevick-Muraca, Eds., pp. 31-51, SPIE Press, Bellingham, WA (2003).
13. M. A. Cohen and J. A. Taylor, "Short-term cardiovascular oscillations in man: measuring and modeling the physiology," *J. Physiol* **542**, 669-683 (2002).
14. Y. L. Pei, H. L. Graber, and R. L. Barbour, "Influence of systematic errors in reference states on image quality and on stability of derived information for DC optical imaging," *Applied Optics* **40**, 5755-5769 (2001).
15. Y. Pei, H. L. Graber, and R. L. Barbour, "A fast reconstruction algorithm for implementation of time-series DC optical tomography," *Proceedings of SPIE Optical Tomography and Spectroscopy of Tissue V*, B. Chance, R. R. Alfano, B. J. Tromberg, M. Tamura, and E. M. Sevick-Muraca, Eds., pp. 236-245, SPIE Press, Bellingham, WA (2003).
16. H. L. Liu, Y. L. Song, K. L. Wondra, X. Jiang, K. A. Concha, and R. P. Mason, "Noninvasive investigation of blood oxygenation dynamics of tumors by near-infrared spectroscopy," *Applied Optics* **39**, 5231-5243 (2000).
17. J. Choi, M. Wolf, V. Toronov, U. Wolf, C. Polzmann, D. Hueber, L. P. Safonova, R. Gupta, A. Michalos, W. Mantulin, and E. Gratton, "Noninvasive determination of the optical properties of adult brain: near-infrared spectroscopy approach," *J. Biomed. Opt.* **9**, 221-229 (2004).
18. D. A. Boas, T. Gaudette, G. Strangman, X. Cheng, J. J. Marota, and J. B. Mandeville, "The accuracy of near infrared spectroscopy and imaging during focal changes in cerebral hemodynamics," *Neuroimage* **13**, 76-90 (2001).
19. H. Obrig, J. Wolf, C. Doge, J. J. Hsieh, U. Dirnagl, and A. Villringer, "Cerebral oxygenation changes during motor and somatosensory stimulation in humans, as measured by near-infrared spectroscopy," *Adv. Exp. Med. Biol.* **388**, 219-224 (1996).
20. M. Hampson, B. S. Peterson, P. Skudlarski, J. C. Gatenby, and J. C. Gore, "Detection of functional connectivity using temporal correlations in fMRI images," *Hum. Brain Mapp.* **15**, 247-262 (2002).

This work was supported by the National Institutes of Health (NIH) under Grants SR21-HL67387-01, 1R21-DK63692 and R41-CA096102, by the US Army under Grant DAMD017-03-C-0018, and by the New York State Department of Health.